Targeted RGD nanoparticles for highly sensitive *in vivo* integrin receptor imaging

Ren-Yen Lin[a†], Kasala Dayananda[a†], Ting-Jung Chen[a], Chiao-Yun Chen[b,c], Gin-Chung Liu[c], Kun-Liang Lin[a] and Yun-Ming Wang[a]*

A new magnetic resonance imaging (MRI) contrast bearing RGD peptide is reported. In this study, ultrasmall superparamagnetic iron oxide (USPIO) nanoparticles with various sizes were prepared. Particles sizes between 6 and 13 nm were tuned by varying the stirring rate. Remarkable negative contrast was observed because USPIO nanoparticles (13.1 ± 2.1 nm) generated high transversal relaxivity r_2 (188 ± 3 mM^{-1} s^{-1}) and saturation magnetization (94 emu g^{-1} Fe). The USPIO nanoparticles were coated with PDA [2-(pyridyldithio)-ethylamine; PDA nanoparticles] containing functional polymer, which can be readily synthesized by Michael addition. The PDA nanoparticles were conjugated with RGD peptide (RGD nanoparticles) for targeting the specific site. The target specificity and high relaxivity allowed RGD nanoparticles to differentiate the expression level of integrin receptor on several cell lines and tumors (MCF-7, A-549, HT-29 and HT-1080) by *in vitro* and *in vivo* MR imaging. Importantly, a remarkable negative contrast ($-51.3 \pm 6.7\%$) was observed for *in vivo* MR imaging of MCF-7 tumor. This result implies that the RGD nanoparticles that greatly enhance the MR imaging are highly sensitive for early stage tumor detection. Copyright © 2012 John Wiley & Sons, Ltd.

Supporting information can be found in the online version of this article

Keywords: superparamagnetic nanoparticles (SPIO); magnetic resonance imaging (MRI); fluorescence; cell; peptide

1. INTRODUCTION

Tumor metastases are most advance stage of cancer and a major cause of death from cancer. Early detection and treatment of cancer significantly minimize the likelihood of cancer metastasis and maximize the success rate of cancer treatment. Integrins are cell surface transmembrane receptors that are involved in adhesive interactions during the metastatic cascade (1). Studies have shown that metastatic cascades are significantly enhanced by the up or down-regulation of integrins expression. For instance, $\alpha_2\beta_1$ and $\alpha_5\beta_1$ integrins responsible for tight contacts during tissue organization are down-regulated during metastatic cascades (2–4). In contrast, $\alpha_v\beta_3$ integrin is up-regulated in metastasis of malignant melanoma cells (5,6). Consequently, $\alpha_v\beta_3$ integrin is the ideal cancer biomarker. The tripeptidic sequence, linear Arg–Gly–Asp (RGD) has been found to be highly selective for $\alpha_v\beta_3$-integrin (7,8). Studies have demonstrated that RGD peptides have potential applications for diagnosis and therapy of cancer. For instance, quantum dot (QD) conjugated with RGD has been successfully used for the detection of tumor vasculature (9). However, the application of QD for *in vivo* imaging of a tumor buried deep inside the body is drastically impeded owing to the light scattering phenomenon (10). In addition, high-quality QD synthesis requires excessive use of heavy metals, raising serious toxicity concerns (11). Over the past decade, many studies have also used the $\alpha_v\beta_3$ specific tripeptide sequence RGD conjugated with a radiolabel to image $\alpha_v\beta_3$ expression using nuclear methods such as PET (12) and SPECT (13). Even though the approach of nuclear imaging of integrin distribution with a radiolabel is very effective and sensitive, the limited spatial resolution of these methods prevents exact localization of the expression of the integrin. Taking into account the high

toxicity, light scattering and spatial resolution problems, magnetic resonance imaging (MRI) is ideally suited for tumor imaging buried deep inside the body with high spatial and temporal resolution. However, one of the major drawbacks of MRI is its low sensitivity. Recently, magnetic nanoparticles are attracting considerable interest as a T_2-weighted MRI contrast agent owing to their inherent biocompatibility and superparamagnetism. Furthermore, unlike Gd(III) complex contrast agents, which are effective only when present in millimolar concentrations, superparamagnetic iron oxide nanoparticles (SPIO nanoparticles) have been found to be effective in nanomolar concentrations (14). The main goal of the current study is to develop a T_2-weighted target-specific MRI contrast agent for $\alpha_v\beta_3$ integrin receptor. For this purpose we have synthesized different sizes of ultrasmall superparamagnetic iron oxide nanoparticles (USPIO

* Correspondence to: Yun-Ming Wang, Department of Biological Science and Technology, Institute of Molecular Medicine and Bioengineering National Chiao Tung University, 75 Bo-Ai Street, Hsinchu, 300, Taiwan.
E-mail: ymwang@mail.nctu.edu.tw

a R.-Y. Lin, K. Dayananda, T.-J. Chen, K.-L. Lin, Y.-M. Wang
Department of Biological Science and Technology, National Chiao Tung University, 75 Bo-Ai Street, Hsinchu 300, Taiwan

b C.-Y. Chen
Department of Radiology, Kaohsiung Medical University, 100 Shih-Chuan 1st Road, Kaohsiung 807, Taiwan

c C.-Y. Chen, G.-C. Liu
Department of Medical Imaging, Kaohsiung Medical University Hospital, Kaohsiung 807, Taiwan

† The first two authors contributed equally.

nanoparticles) conjugated with simplest RGD, which was found to recognize at least eight integrin receptors out of 25.

Conventionally, SPIO nanoparticles are synthesized by the co-precipitation method with a broad size distribution and poor crystallinity. Consequently, the quality of nanoparticles required for strong negative contrast effects in T_2-weighted MR imaging was far below that required. Recently, the nonhydrolytic thermal-decomposition method has drawn intense attention (15–17). This method allows synthetic control of some of the important features of magnetic nanoparticles, for instance, magnetic dopants, magneto-crystalline phases, size, magnetization, spin–spin relaxivity and surface states (15,18). The size control of nanoparticles has been recognized to be equally important to shape control, which is achieved by varying the concentration of activation reagents (17–20). However, the major drawback of the nonhydrolytic thermal-decomposition method is the use of hydrophobic surfactants in the synthetic process, which results in a hydrophobic coating on the nanoparticle surface. To avoid the nonspecific uptake and to improve the selectivity of the targeting tissue, small and appropriate nanoparticles coated with biocompatible polymers and conjugated with bio-probes are highly desirable (21–24). Several biocompatible synthetics and natural polymers have been employed to coat the surface of SPIO nanoparticles in order to achieve high colloidal stability and dispersibility in aqueous biofluids. Those polymers include poly(ethylene glycol) (PEG) (25–27), dextrans (23,26), poly(lactic-co-glycolic acid) (PLGA) (28) and some co-polymers (29). They are known to be biocompatible and also improve the dispersion of SPIO nanoparticles in an aqueous environment. In addition, water-soluble anti-biofouling PEG polymer coating effectively reduces the reticuloendothelial system uptake (30,31), subsequently prolonging the half-life of SPIO in the blood (32,33). A longer blood half-life of SPIO allows for specific accumulation in tumor by an enhanced permeability and retention effect.

Recently, our group reported the use of iron oxide nanoparticles conjugated with bio-probes such as densyl hapten (34), herceptin (35) and folic acid (36) for noninvasive MR imaging. In this study, the USPIO nanoparticles are synthesized by thermolysis of ferric oleate. The USPIO nanoparticles were coated with mPPDA-silane [PDA nanoparticles; 2-(pyridyldithio)-ethylamine]. Subsequently, in the thiol-disulfur bond exchange reaction, the PDA nanoparticles were conjugated with the bio-marker of RGD peptide (RGD nanoparticles) to increase the receptor-mediated internalization in the targeted cancer cells. The resulting nanoparticles were characterized by dynamic light scattering (DLS), Fourier transform-infrared (FT-IR), a 20 MHz relaxometer, a 3.0 T magnetic resonance imager, a superconducting quantum interference device (SQUID) and transmission electron microscopy (TEM). Moreover, the cytotoxicity of RGD nanoparticles to cancer cells was also investigated. Finally, *in vitro* and *in vivo* MR imaging studies are carried out using various amounts of integrin expression receptors of cancer cell lines and tumors with RGD nanoparticles.

2. RESULTS AND DISCUSSION

In this study, we modified the surface of USPIO nanoparticles by conjugating them with linear RGD peptide (Ac-CKGRGD). Scheme 1 illustrates the synthetic route of the RGD nanoparticles. Initially, the USPIO nanoparticles were synthesized by modification of the reported procedure (37). The various sizes of nanoparticles were formed and regulated by mechanical
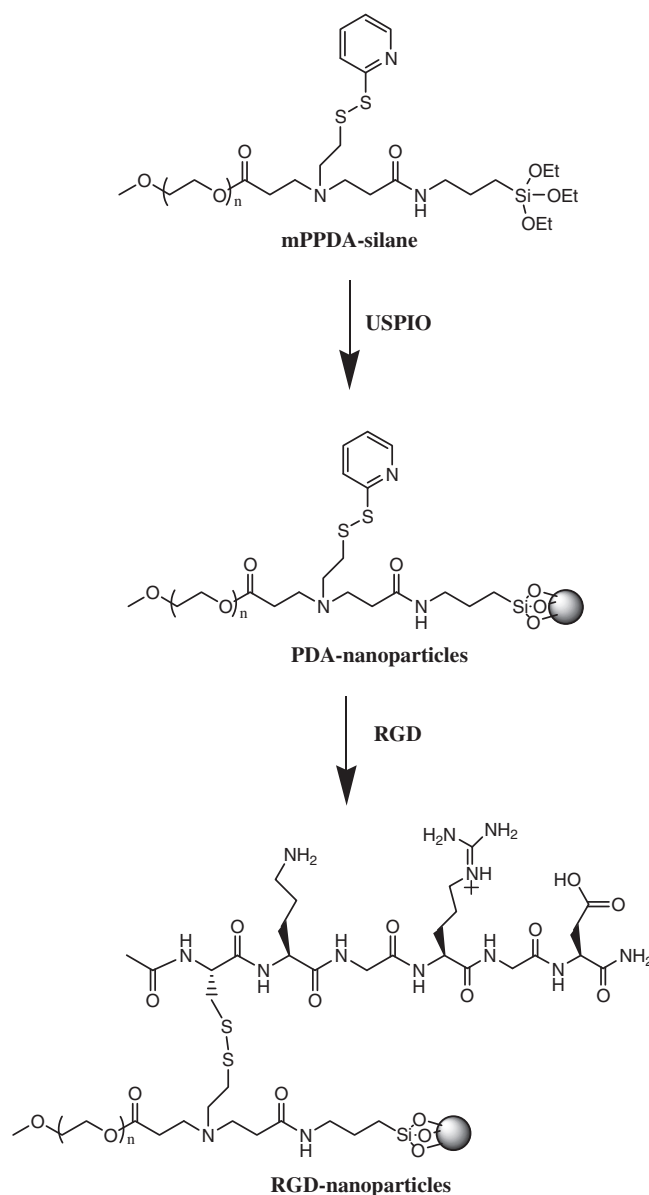
**Scheme 1.** Synthetic scheme of RGD nanoparticles.

agitation of the reaction. The diameters of the USPIO nanoparticles were estimated by TEM, as shown in Fig. 1. The diameters resulting from varied stirring rates (300, 600 and 900 rpm) were 13.1 ± 2.1, 9.2 ± 1.1 and 6.7 ± 1.3 nm, respectively. The monodisperse nanoparticles can be observed in Fig. 1(A–C) and the enlarged images are shown in Fig. 1(D–F). Based on TEM results we can conclude that higher speed agitation resulted in the formation of smaller nanoparticles. These results are similar to those for magnetite nanoparticles, obtained by coprecipitation (36). Hence, the mechanical agitation affects the formation of particle size. Additionally, the USPIO nanoparticle surfaces were modified with mPPDA-silane (PDA nanoparticles) (Scheme S1, Supporting Information) and coated with RGD peptide (RGD nanoparticles).

The USPIO nanoparticles were coated with oleic acid and were confirmed by FT-IR (Fig. S1, Supporting Information). The C&dbond;O stretching (~1700 cm^{-1}) could be observed in the spectra of oleic acid and USPIO nanoparticles (15,16). In addition, the magnetic sensitivity of the synthesized USPIO nanoparticles
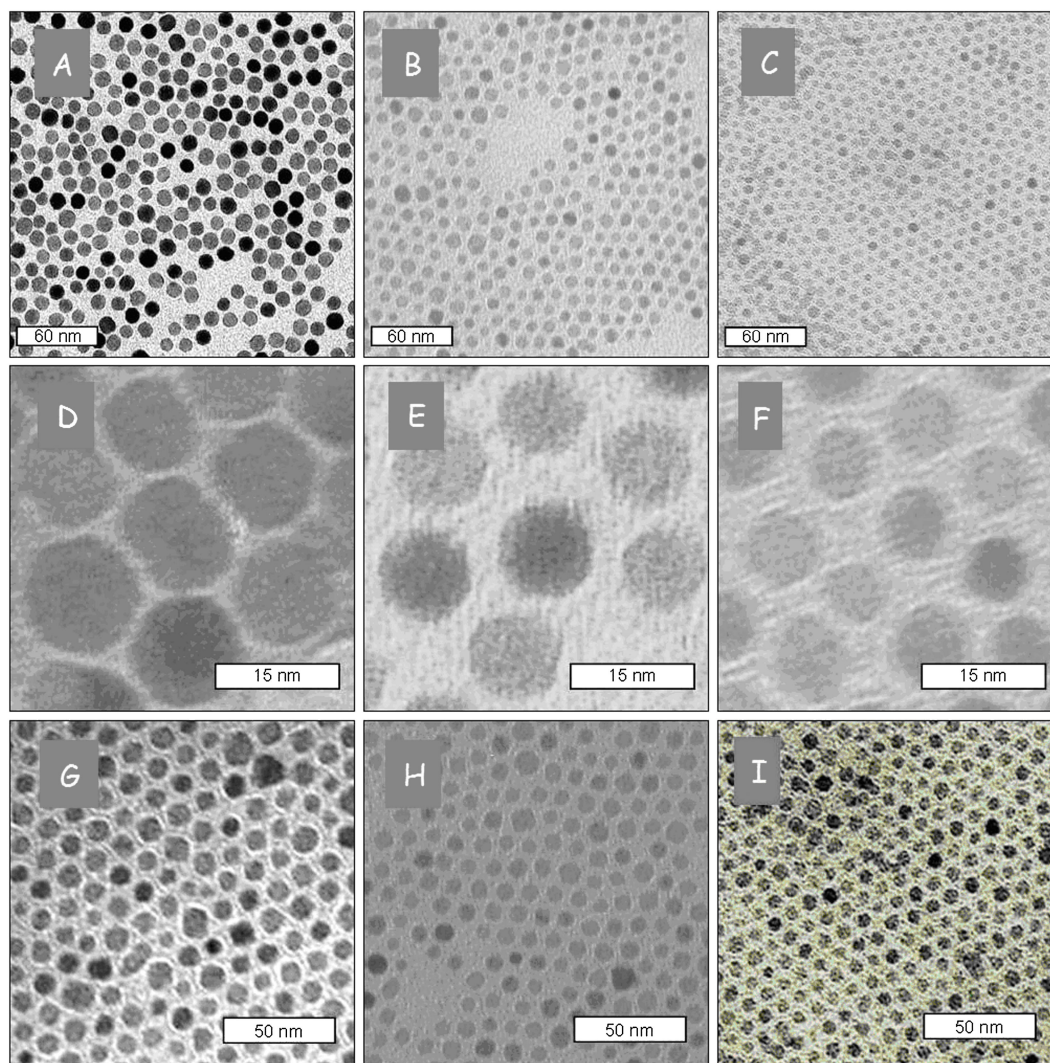
Figure 1. (A–C) Transmission electron microscopy (TEM) images of ultrasmall superparamagnetic iron oxide (USPIO) nanoparticles; (D–F) enlarged images of USPIO nanoparticles; (A and D) 13.1 ± 2.1, (B and E) 9.2 ± 1.1 (C and F) and 6.7 ± 1.3 nm. (G–I) TEM images of PDA nanoparticles.

was examined using a SQUID magnetometer. The USPIO nanoparticles displayed superparemagnetic behaviors without any magnetic hysteresis. The 13.1 nm USPIO nanoparticles exhibited the highest mass magnetization value ($94 \, \mathrm{emu \, g^{-1}}$ Fe). The
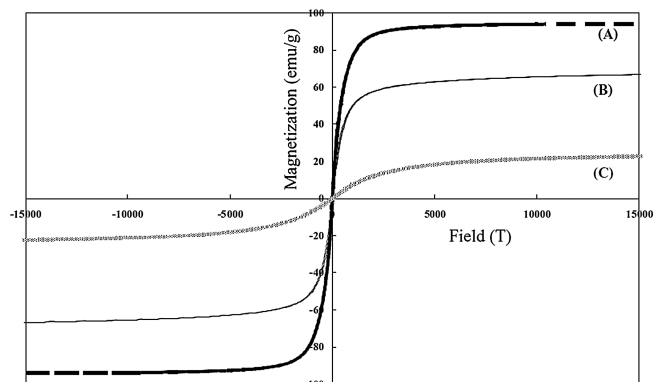
Figure 2. Variation of the magnetization of (A) 13.1 nm ultrasmall superparamagnetic iron oxide (USPIO) nanoparticles; (B) 9.2 nm USPIO nanoparticles; and (C) 6.7 nm USPIO nanoparticles.

magnetization value was reduced to 79 and $63 \, \mathrm{emu \, g^{-1}}$ Fe for 9.2 and 6.7 nm, respectively, as shown in Fig. 2. The tendency of magnetization value depends on the size of USPIO nanoparticles. Moreover, the coercivity (H_C) values of 13.1 ± 2.1, 9.2 ± 1.1, and 6.7 ± 1.3 nm USPIO nanoparticles were 1, 2 and 1 Oe, respectively. These results are similar to those of magnetism-engineered iron oxide nanocrystals (15,18).

In order to introduce the hydrophilic moiety on the surface of USPIO nanoparticles, the mPPDA-silane was synthesized via a Michael addition type reaction using mPEG acrylate, APTES acrylate and PDA in dichloromethane at 40 °C for 72 h. The modified polymer was confirmed by ^{1}H NMR. Unlike copolymer (30,31), this synthesis utilized Michael addition (38) to combine all the functional moieties. Then the USPIO nanoparticles were coated with mPPDA-silane instead of oleic acid. The PDA nanoparticles were also confirmed by FT-IR (Fig. S1). The band at $1100 \, \mathrm{cm^{-1}}$ corresponds to the C–O–C stretching vibration of PEG. The band at $1400 \, \mathrm{cm^{-1}}$ was attributed to C&dbond;C stretching. The band at $1600 \, \mathrm{cm^{-1}}$ was assigned to the C&dbond;N stretching band of PDA. Compared with other promising bifunctional PEG-silanes (39–42), mPPDA-silane was easily obtained through a single step of the Michael addition-type modification.
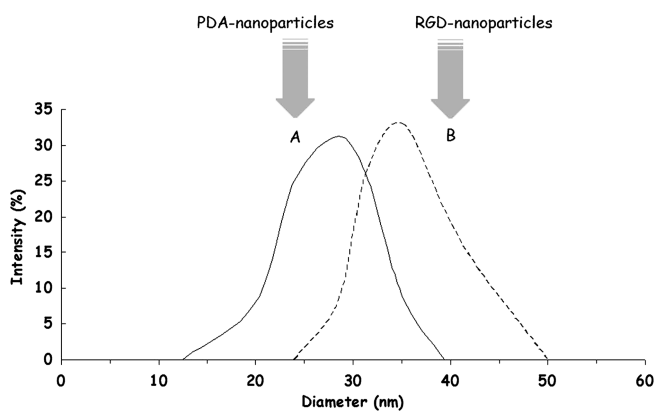
Figure 3. Hydrodynamic sizes of the 13.1 nm ultrasmall superparamagnetic iron oxide nanoparticles coated with mPPDA polymer (A) and then conjugated with RGD (B).

The RGD peptide was conjugated with PDA nanoparticles, and the adduct was confirmed by the BCA protein assay kit (Fig. S2). In addition, conjugation of RGD peptide was examined using a UV–vis spectrophotometer. The UV–vis spectrum showed a distinctive peak at 343 nm corresponding to the 2-mercaptopyridine (2-MP; Fig. S3) (38). Since the terminal thiol of peptides replaced the dithiopyridine side group, the 2-MP was released from the polymer chain. The above results provide clear evidence for the RGD peptide conjugated with nanoparticles.

The diameter of PDA nanoparticles was estimated by TEM image, as shown in Fig. 1(G–I). No obvious change in core size can be detected using TEM after the surface modification of

USPIO nanoparticles. This result indicated that the core of nanoparticles retained their original form. Furthermore, the coating layer of the nanoparticles was characterized by DLS. The typical size distributions of PDA nanoparticles and RGD nanoparticles were measured as shown in Fig. 3. After the surface modification with mPPDA-silane, the average hydrodynamic diameter of 13.1 nm USPIO nanoparticles increased to 29.9 ± 3.5 nm. Subsequently, the PDA nanoparticles were conjugated with RGD peptide, with the average diameter further augmented to 36.5 ± 4.2 nm. It was evident that the surface of USPIO nanoparticles was modified with mPPDA-silane and RGD peptide. Furthermore, the ζ-potential value of particle surface was also measured at each step. After mPPDA-silane coating, there was only a slight change at ζ-potential from 6.6 ± 0.8 to 4.3 ± 0.6 mV. However, the ζ-potential value remarkably increased to 21.8 ± 0.4 mV for RGD nanoparticles.

Different USPIO nanoparticles and their physicochemical characteristics are summarized in Table 1. The r_2 relaxivity values of 13.1, 9.2 and 6.7 nm RGD nanoparticles were 188 ± 12, 113 ± 9, and 106 ± 5 $mM^{-1}\,s^{-1}$, respectively, at 37.0 ± 0.1 °C and 20 MHz. Compared with a magnetic nanocrystal using $Fe(acetylacetonate)_3$ as a precursor (15,18), the r_2 relaxivity values of RGD nanoparticles for different particles size were similar to those of the above magnetic nanocrystals.

To examine the colloidal stability of RGD nanoparticles under physiological conditions, nanoparticles dispersed in various pH solutions were investigated. As shown in Fig. S4, the RGD nanoparticles were well-dispersed in Phosphate buffered saline (PBS) buffer solution (pH 7.4) as well as in the pH range from 4 to 10.

Furthermore, the storage life and the stability of RGD nanoparticles were also estimated by DLS, as shown in Fig. 4(A). The average

**Table 1.** The relaxivity and diameter of USPIO, PDA and RGD nanoparticles

Sample	TEM (nm)	DLS (nm)	r_1 ($mM^{-1}\,s^{-1}$)	r_2 ($mM^{-1}\,s^{-1}$)
USPIO nanoparticles	13.1 ± 2.1			
	9.2 ± 1.1			
	6.7 ± 1.3			
PDA nanoparticles	13.1 ± 2.1	29.9 ± 3.5		
	9.2 ± 1.1	22.3 ± 2.7		
	6.7 ± 1.3	15.3 ± 1.7		
RGD nanoparticles	13.1 ± 2.1	36.5 ± 4.2	28.6 ± 0.9	188 ± 12
	9.2 ± 1.1	27.1 ± 3.4	27.5 ± 1.4	113 ± 9
	6.7 ± 1.3	24.9 ± 2.2	15.2 ± 0.8	106 ± 5
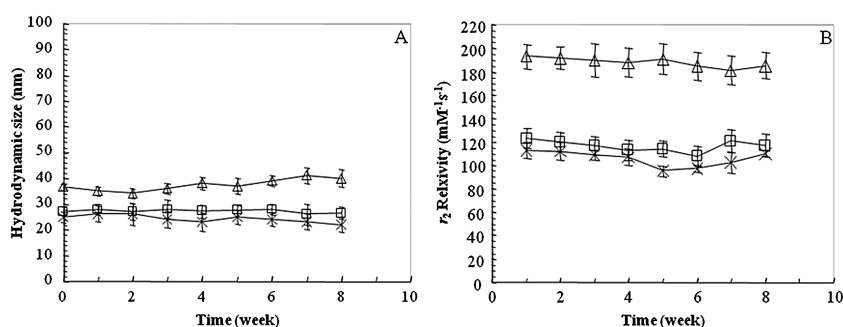
Figure 4. Stability test: (A) hydrodynamic diameter distribution with time of three different RGD nanoparticles at 25.0 ± 0.1 °C; (B) relaxivity (r_2) with time of each RGD nanoparticle at 37.0 ± 0.1 °C and 20 MHz; (Δ) 13.1 nm core of RGD nanoparticles, (Δ) 9.2 nm core of RGD nanoparticles and (×) 6.8 nm core of RGD nanoparticles.
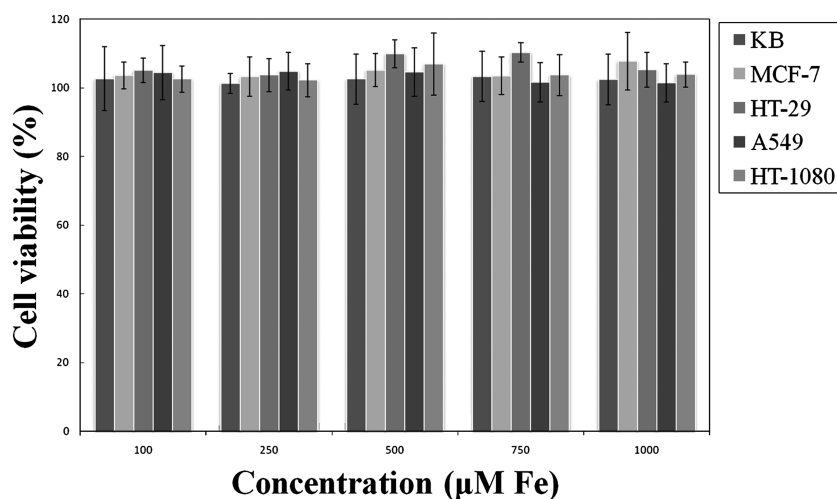
Figure 5. Cytotoxicity of RGD nanoparticles incubated with KB (red), MCF-7 (yellow), A549 (blue), HT-29 (green) and HT-1080 (purple) for 48 h. Concentration dependence (100–1000 μM Fe) of MTT assay graph observed *in vitro* cell viability after incubation of 13.1 nm RGD nanoparticles.
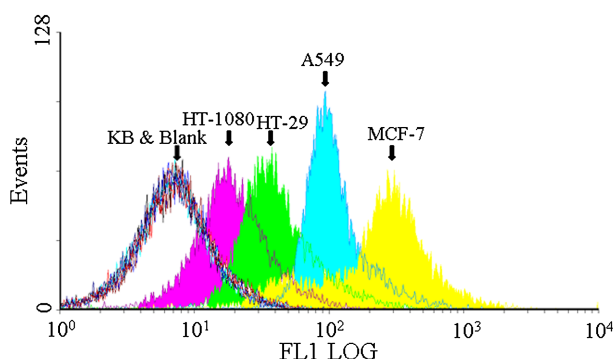

Figure 6. Fluorescence-activated cell sorting analysis of FITC-RGD nanoparticles targeted to positive (MCF-7, A-549, HT-29 and HT-1080) and negative (KB) cells. The blank comprises the positive and negative cells without FITC-RGD nanoparticle incubation.

hydrodynamic diameter of RGD nanoparticles slightly changed after 2 months in PBS buffer solution at pH 7.4. In addition, the r_2 relaxivity values had no significant difference for the same period of time at $37.0 \pm 0.1\,°C$ and 20 MHz, as shown in Fig. 4(B). The RGD peptide containing polymer could improve the stability of the nanoparticles. These results were also similar to those of CLIO-dansyl (34), herceptin nanoparticles (35) and SPIO-PEG-FA (36). Hence, the RGD nanoparticles were extremely stable.

(3-(4,5-dimethylthiazolyl-2)-2,5-diphenyltetrazolium bromide (MTT) assays using the MCF-7, A-549, HT-29, HT-1080 (positive cells) and KB (negative cell) cell lines were performed to evaluate the potential cytotoxicity of the RGD nanoparticles. As shown in Fig. 5, more than 90% cell viability was observed even after 48 h of incubation with high concentrations of RGD nanoparticles. These results indicated that the RGD nanoparticles did not inhibit cell growth from 100 to 1000 μM Fe concentrations. Therefore, RGD nanoparticles exhibited a low cytotoxicity.

To evaluate the expression level of the integrin receptor by flow cytometry, the over-expressing cancer cells (MCF-7, A-549, HT-29 and HT-1080) were incubated with RGD nanoparticles (0.5 mM Fe), as shown in Fig. 6. Our results showed that the curve for Fluorescein isothiocyanate (FITC)-RGD nanoparticles with MCF-7 and A-549 cells (yellow and blue area) moved from 10^1 to nearly 10^3; the curve shifted slightly with for HT-29 (green area) and HT-1080 (purple area). No curve shift was observed
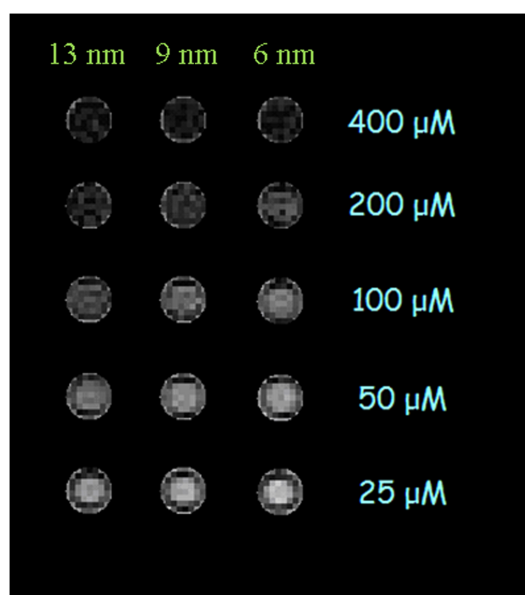
Figure 7. T_2-weighted MR images of RGD nanoparticles by various iron concentrations and different core; the sizes of nanoparticles core are shown above each image.
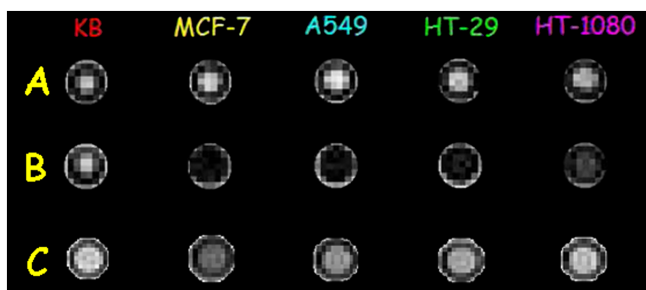
Figure 8. *In vivo* T_2-weighted MR images of positive and negative cell lines for integrin expression after treatment with or without 0.2 mM of RGD nanoparticles (13.1 ± 2.0 nm). (A) Without RGD nanoparticles; (B) after incubation with RGD nanoparticles; (C) after incubation with USPIO nanoparticles.

with the KB cells (black line). These results indicated that the expression level of $\alpha_v\beta_3$ was higher in MCF-7 and A549 cells, whereas the expression level was lower in HT1080 and HT-29 cells.

The T_2-weighted MR imaging of three different sizes of RGD nanoparticles (13.1, 9.2, and 6.7 nm) in PBS buffer solution at the various concentrations (400, 200, 100, 50 and 25 μM) was preformed at 3.0 T with an MR scanner. Figure 7 shows that a gradual decrease in the negative contrast was observed as the concentration of iron oxide decreased. However, the 9.2 nm RGD nanoparticles had no MR negative contrast at 25 μM; neither did 6.7 nm RGD nanoparticles at a concentration less than 50 μM. The 13.1 nm RGD nanoparticles had extremely high negative

imaging contrast, even at very low concentration. In other words, we have developed high-sensitivity T_2 contrast agent RGD nanoparticles (13.1 nm) with high relaxivity 188 ± 12 mM^{-1} s^{-1}. Among RGD nanoparticles with various sizes, 13.1 nm RGD nanoparticles had the strongest negative contrast effect. Therefore, *in vitro* or *in vivo* MR imaging studies using a low dose of contrast agent were performed.

The receptor-targeting specificity of the RGD nanoparticles (13.1 ± 2 nm) to the integrin expressing cells was further examined using T_2-weighted MR imaging, as shown in Fig. 8. The RGD nanoparticles were incubated with the integrin-negative cells (KB) and integrin-positive cells (MCF-7, A-549, HT-29 and HT-1080) for 0.5 h at 37.0 ± 0.1 °C. The negative signal contrasts for the positive MCF-7, A-549, HT-29 and HT-1080 cell lines were 78.8 ± 5.6, 65.2 ± 7.1, 47.1 ± 3.2 and 14.2 ± 2.0%, respectively. However, a minute signal contrast for the negative cells (KB cell; 4.0 ± 0.7%) was observed. After the uptake of RGD nanoparticles, the contrasts of positive cells were significantly lower than that of negative cell. Because of the lack of integrin expression, the signal intensity of KB cell line was not enhanced. The tendency of integrin expression level was differentiated for MCF-7, A-549, HT-29 and HT-1080 cell lines.

Additionally, tumor-bearing mice were prepared by subcutaneous injection of the positive cells (MCF-7, A549, HT-29 and HT-1080) and negative cell (KB) into the right and left lateral thighs, respectively. The *in vivo* MR imaging was performed at predetermined time intervals after the intravenous injection of USPIO nanoparticles and RGD nanoparticles (13.1 ± 2.1 nm, 15 μmol Fe kg^{-1}), respectively. The T_2-weighted MR images were performed over 0.4–24 h as shown in Fig. 9. The region-of-
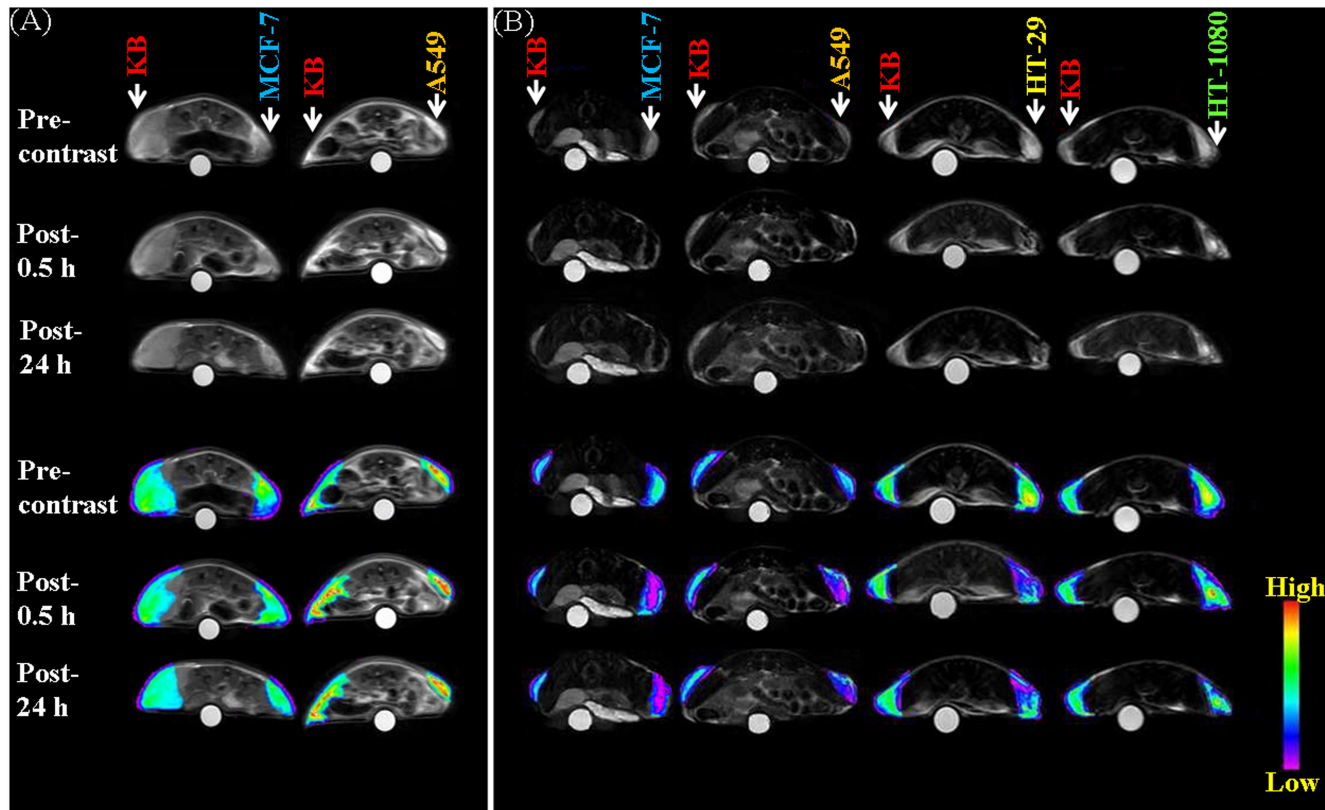

Figure 9. T_2-weighted MR images of tumor cell implanted mice at 3.0 T and the color mapped before and after injection (0.5 h and 24 h). (A) Ultrasmall superparamagnetic iron oxide nanoparticles; (B) RGD nanoparticles (13.1 ± 0.5 nm) (15 μmol Fe kg^{-1}). The gray area in the MR images shows tumors (arrow) and the color mapping image indicates details of signal contrast.

interest analysis of the tumors (MCF-7, A549, HT-29 and HT-1080) indicated that the negative contrasts were 31.5 ± 8.3, 23.2 ± 4.1, 15.6 ± 5.5 and 8.3 ± 3.1, respectively, for 3 h. In other words, the RGD nanoparticles have specifically targeted to integrin receptor-expressing tumors. In addition, the *in vivo* MR imaging of RGD nanoparticles was studied at different time intervals. Figure S5 shows the negative contrast for the positive tumor (MCF-7, A549, HT-29 and HT-1080). In contrast, no negative contrast was observed for the USPIO nanoparticles. Moreover, the tendency towards negative contrast of *in vivo* imaging is in good agreement with flow cytometry analysis and *in vitro* MR imaging. These results indicated that the receptor-specific RGD nanoparticles could differentiate cell lines according to their integrin expression level. Also, the RGD nanoparticles exhibited an effectively accumulating ability in low or high integrin expression tumors. In addition, the tendency of negative contrast decreased over 24 h, owing to the excretion of nanoparticles from the body.

The specific targeting ability of RGD nanoparticles on the cellular level was further examined using confocal fluorescence microscopy and FITC-labeled nanoparticles. MCF-7 cells were incubated with FITC-USPIO nanoparticles, FITC-RGD nanoparticles and FITC-RGD nanoparticles with four-fold excess free RGD, respectively. After 1 h of incubation, minute uptake of RGD nanoparticles was observed, as shown in Fig. 10. However, there was no remarkable uptake for plain USPIO nanoparticles and RGD nanopartilces with four-fold excess free RGD. After 3 h of incubation, the differences in nanoparticles uptake among these conditions were clearly visualized, as shown in Figure 10. Blocking the integrin receptor with free RGD effectively reduced the amount of yellow granules in the cytoplasm of MCF-7. These results indicated that accumulation of these particles faithfully reflected their integrin binding (43). This clearly demonstrates that RGD nanoparticles have the ability to target integrin receptors in the MCF-7 tumor cell lines. Furthermore, the uptake of USPIO nanoparticles and RGD nanoparticles in MCF-7 tumors was histologically examined using Prussian blue staining. Tumor-bearing mice were sacrificed 3 h post- injection and the tumors were sectioned and subjected to histological studies, as shown in Fig. 11. Blue spots were observed in the tumor slices injected with RGD nanoparticles, but there was no significant uptake for plain USPIO nanoparticles. These results imply that the accumulation of RGD nanoparticles was specifically mediated by integrin binding. Additionally, they clearly demonstrate that the RGD nanoparticles were localized on the integrin expressing tumor vasculature with minute macrophage uptake.
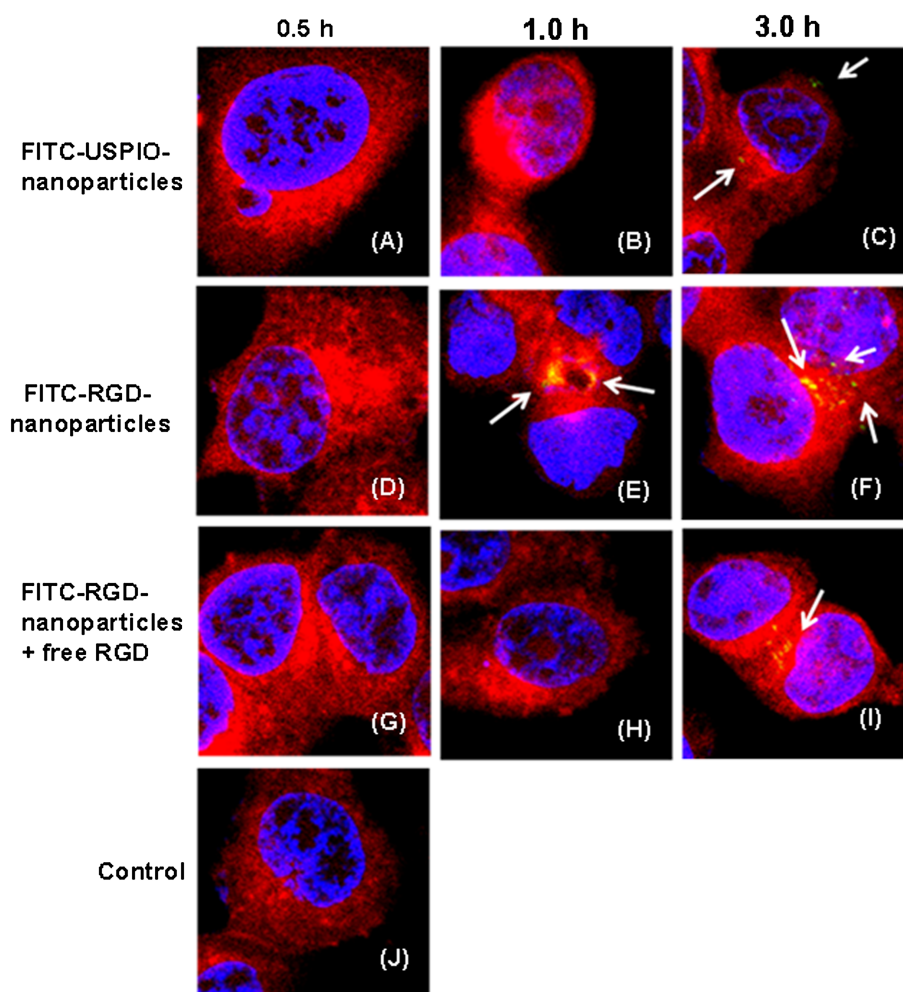
Figure 10. Confocal fluorescence microscopic images of MCF-7 cells incubated with FITC-USPIO nanoparticles (A–C), FITC-RGD nanoparticles (D–F), and FITC-RGD nanoparticles with four-fold excess of free RGD (G–I) at an iron concentration of 15 µmol Fe kg^{-1} of growth medium for predetermined time intervals (0.5, 1.0, and 3.0 h). Control cells (MCF-7) were not treated with FITC-USPIO nanoparticles, as shown in (J). Major uptake of FITC-RGD nanoparticles (yellow granules) compared with those of FITC-USPIO nanoparticles and FITC-RGD nanoparticles with four-fold excess of free RGD was observed.
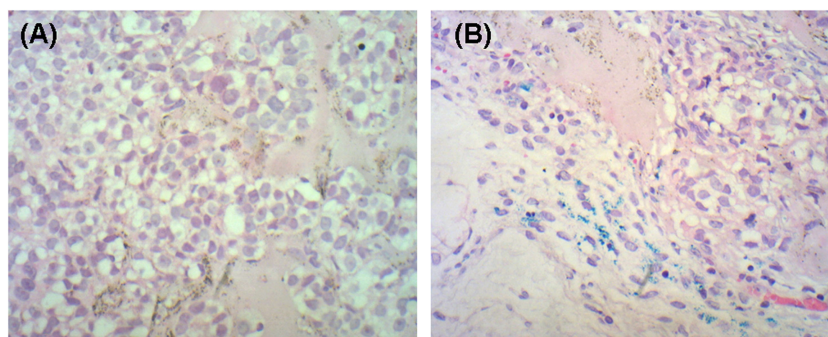
Figure 11. Prussian-blue staining images of the MCF-7 tumor treated with (A) ultrasmall superparamagnetic iron oxide nanoparticles, and (B) RGD nanoparticles.

3. CONCLUSION

In summary, we presented an efficient and receptor-specific magnetic nano-probe for the *in vivo* MR imaging application. Various sizes of USPIO nanoparticles were successfully synthesized and tuned using the stirring rates. The surface of USPIO nanoparticles was coated with a biocompatible polymer and conjugated with bio-probe (RGD nanoparticles). The results showed the RGD nanoparticles well dispersed over a wide range of pH, as well as no hysteresis, superparamagnetic properties, high relaxivity and low cytotoxicity in different cell lines. Targeting of RGD nanoparticles was observed using *in vitro* and *in vivo* MR imaging studies. In addition, RGD nanoparticles had the ability to differentiate human cancer cells with different integrin expression levels such as MCF-7, A549, HT-29 and HT-1080 cells and tumors. These results indicate that the RGD nanoparticles can potentially be used as a contrast agent for MRI.

4. EXPERIMENTAL METHOD

4.1. Materials and instruments

Methoxy poly(ethylene glycol) (mPEG, M_n =750), iron chloride (FeCl$_3$·6H$_2$O), were purchased from Sigma-Aldrich (St Louis, MO, USA). 2,2′-Dipyridyl disulfide (DPDS, 98%), 2-mercaptoethylamine hydrochloride (98%), 1-octadecene (ODE, 90%) and acryloyl chloride were purchased from Alfa Aesar (Ward Hill, MA, USA) and used as received. 3-Aminopropyltriethoxysilane (APTES, 98%) was purchased from Fluka (Buchs SG, Schweiz). *N*-Methyl-2-pyrrolidone (NMP, 100%) was purchased from TEDIA (Fairfield, OH, USA). Reagents for peptide synthesis were purchased from Novabiochem (Darmstadt, Germany) and Sigma-Aldrich (St Louis, MO, USA). BCA protein assay reagent kit (bicinchoninic acid) was purchased from Pierce (Rockford, IL, USA). Matrigel was purchased from BD Biosciences, (San Jose, CA, USA). SPECTRUM molecular porous membrane tubing was purchased from Spectrum Laboratories Inc. All chemicals were used directly without any further purification. ^{1}H (400 MHz) NMR spectra were recorded on a Varian Gemini 400 MHz spectrometer (Agilent Technologies, CA, USA). The HPLC experiments were performed on an Amersham ÄKTAbasic (GE Healthcare, NJ, USA) 10 instrument equipped with an Amersham UV-900 detector (GE Healthcare, NJ, USA) and Amersham Frac-920 fraction collector (GE Healthcare, USA). Supelco RP-C$_{18}$ columns (Sigma-Aldrich, St Louis, MO, USA; 5 μm, 4.6 × 250 mm and 5 μm, 10 × 250 mm) were used. LC-mass spectral analyses were performed with Waters Micromass-ZQ mass spectrometry (Waters, MA, USA).

4.2. Syntheses

4.2.1. Synthesis of USPIO nanoparticles

Briefly, iron oleate complex was prepared by iron chloride and sodium oleate heated to 70 °C for 4 h in a mixture of ethanol, distilled water and *n*-hexane (16). The resulting solution was washed three times with distilled water and the product was obtained by evaporating organic solvents. Followed by iron oleate complex (3.1 g, 3.3 mmol) and oleic acid (0.4 ml, 1.6 mmol) were dissolved in 1-octadecene (20 ml). Subsequently, the reaction mixture was degassed under vacuum at 120 °C for 1 h, in order to remove excess water and then the temperature rose to 300 °C with a constant heating rate of 3.3 °C/min, and then kept at that temperature for 1 h (37). The homogenized brown solution was darkened when the reaction temperature reached 300 °C. The resulting solution was allowed to cool down to room temperature, and then 50 ml of ethanol was added to this solution to precipitate the USPIO nanoparticles. The USPIO nanoparticles were separated by centrifugation and stored in toluene. The particle sizes could be controlled through a range of stirring rates without changing iron and surfactant concentration or using any activation reagent. The iron concentration of the USPIO nanoparticles was spectrophotometrically determined as previously described (44).

4.2.2. Synthesis of 2-(pyridyldithio)-ethylamine (1)

Briefly, 2-mercaptoethylamine hydrochloride (2.29 g, 20 mmol) was dissolved in methanol (17.5 ml) and added dropwise to a stirred solution of DPDS (8.82 g, 40 mmol) dissolved in methanol (41.6 ml containing 1.6 ml of glacial acetic acid). The reaction was kept under an argon atmosphere to minimize free thiol oxidation. After 48 h, the mixture was concentrated under reduced pressure to give approximately 10–15 ml of yellow oil. The product was precipitated by the addition of 100 ml cold ether. Redissolving in methanol (20 ml) and precipitating with cold ether (100 ml), repeated six times, gave a white powder. Sodium hydroxide (0.38 g, 9.6 mmol) was dissolved in 1 ml of water and quickly added to 2-(pyridyldithio)-ethylamine hydrochloride (1.95 g, 8.8 mmol) dissolved in 2 ml of water. The solution was briefly agitated and allowed to stand for 15 min. The product (PDA free base phase) was separated by draining from the tube bottom. ^{1}H NMR (400 MHz, D$_2$O) δ = 3.05 (t, *J* = 6.8 Hz, 2H, -CH$_2$-

CH$_2$-N), 3.06 (t, *J* = 7.0 Hz, 2H, -CH$_2$-*CH$_2$*-S-); pyridyl-2-thiol: 7.27 (1H), 7.68(1H), 7.76(1H) and 8.37(1H). MS ESI, for C$_7$H$_{11}$N$_2$S$_2$: calculated, 186.3; found, 187.1.

4.2.3. Synthesis of mPEG-acrylate (**2**)

Methoxy poly(ethylene glycol) (mPEG, *M$_n$* = 750) (75 g, 100 mmol) was dissolved in dry dichloromethane (100 ml), and then triethylamine (20 ml, 144 mmol) was added. The temperature of the reaction mixture was maintained between 0 and 10 °C. Acryloyl chloride (10.8 ml, 108 mmol) was added slowly to the above mixture. Upon completion of the addition, the reaction mixture was allowed to warm up to room temperature and it was stirred at room temperature for 48 h. Then the residue of the triethylamine hydrochloride salt was removed by filtering and the filtrate was precipitated in cold hexane. The resulting product was filtered and dried under vacuum for overnight. The crude product was purified by silica-gel chromatography (eluent: chloroform–methanol, 9:1). ^{1}H NMR (400 MHz, D$_2$O) δ = 0.67 (t, *J* = 7.1 Hz, 2H; C–*CH$_2$*–Si), 1.19 (q, *J* = 8.1 Hz, 9H; *CH$_3$*–CH$_2$–O), 1.65 (m, *J* = 7.5 Hz, 2H; C–*CH$_2$*–C), 3.32 (t, *J* = 7.1 Hz, 2H; C–*CH$_2$*–N), 3.81 (q, *J* = 8.4 Hz, 6H; C–*CH$_2$*–O); acryl group, 5.56 (1H), 6.15 (1H), 6.37 (1H). IR (KBr): 1724 cm^{-1} [*v* (C&dbond;O) stretching].

4.2.4. Synthesis of APTES-acrylate (**3**)

Aminopropyltriethoxysilane (APTES) (10 g, 45 mmol) and triethylamine (13 ml, 93 mmol) were cooled in an ice bath, and then acryloyl chloride (4.1 g, 45 mmol) was slowly added. The stirring was continued for 3 h at room temperature and then the solvent was evaporated. The resulting compound was purified by silica-gel chromatography (eluent: chloroform–methanol, 9:1). ^{1}H NMR (400 MHz, CDCl$_3$) δ = 0.67 (t, *J* = 7.1 Hz, 2H; C–*CH$_2$*–Si), 1.19 (q, *J* = 8.1 Hz, 9H; *CH$_3$*–CH$_2$–O), 1.65 (m, *J* = 7.5 Hz, 2H; C–*CH$_2$*–C), 3.32 (t, *J* = 7.1 Hz, 2H; C–*CH$_2$*–N), 3.81 (q, *J* = 8.4 Hz, 6H; C–*CH$_2$*–O); acryl group, 5.56 (1H), 6.15 (1H), 6.37 (1H). IR (KBr): 1633, 1732 cm^{-1} [*v*(C&dbond;O) stretching], 1553 cm^{-1} (2º-NH bending), 3070 cm^{-1} (2º-NH bending), MS ESI$^+$ for C$_{12}$H$_{26}$ClNO$_4$Si, calculated, 310.9; found, 311.0.

4.2.5. Synthesis of N-APTES-N-mPEG-PDA (mPPDA-silane)

APTES-Ac (1.4 g, 5 mmol), mPEG-Ac (4.2 g, 5 mmol) and PDA (0.9 g, 5 mmol) were dissolved in dry dichloromethane (20 ml), and then triethylamine (0.7 ml, 5 mmol) was added. The resulting mixture was stirred under nitrogen atmosphere at 40 °C for 72 h. Finally, the product was precipitated in cold hexane. ^{1}H NMR (400 MHz, CDCl$_3$) δ = 0.64 (t, *J* = 7.9 Hz, 2H; Si–*CH$_2$*–), 1.24 (t, *J* = 7.4 Hz, 9H; CH$_2$–*CH$_3$*), 1.66 (p, *J* = 8.1 Hz, 2H; C–*CH$_2$*–C), 2.27 [t, *J* = 7.1 Hz, 2H; –C–*CH$_2$*–(C&dbond;O)–N], 2.47 [t, *J* = 7.2 Hz, 2H, –C–*CH$_2$*–(C&dbond;O)–O], 2.65 (m, 4H; –N–*CH$_2$*–*CH$_2$*–S–), 2.65 [m, 2H, N–*CH$_2$*–C–(C&dbond;O)–N], 2.85 [t, *J* = 7.0 Hz, 2H; N–*CH$_2$*–C–(C&dbond;O)–O], 3.37 (t, *J* = 6.8 Hz, 2H; –C–*CH$_2$*–NH–), 3.45 (s, 3H, –O–*CH$_3$*), 3.54–3.70 [m, ~70H, –(*CH$_2$*–O–*CH$_2$*)$_n$–], 3.83 (q, 6H, –O–*CH$_2$*–CH$_3$*); pyridyl-2-thiol, 7.11 (1H), 7.61 (2H) and 8.45 (1H). IR (KBr): 1731 cm^{-1} [*v*(C&dbond;O) region], 1400–1600 cm^{-1} (2-subst. pyridine).

4.2.6. Synthesis of peptide

The RGD peptide (Ac-CKGRGD) was synthesized on an automatic solid-phase peptide synthesizer (PS3, Rainin, Woburn, MA, USA) as C-terminal on the Rink Amide AM resin (0.63 mmol g^{-1} loading) using standard Fmoc chemistry. The side chain protecting groups of trifunctional amino acids were labile trifluoroacetic acid. The peptide was synthesized on a 0.128 mmol scale using a 4-fold molar excess of Fmoc-protected amino acids (0.512 mmol) that were activated using 4-fold excess of PyBoP in the presence of NMM (20% v/v) in DMF. N^{α}-Fmoc protecting groups were removed by treating the resin-attached peptide with piperidine (20% v/v) in DMF. The resin-bound polypeptide chain was cleaved from the solid support by treatment with a cocktail of trifluoroacetic acid–H$_2$O–triisopropylsilane (95:2.5:2.5%, 10 ml) for 120 min. The RGD peptide was purified by preparative HPLC, and its molecular weight was identified by mass spectrometry. MS ESI$^+$ for C$_{25}$H$_{45}$N$_{11}$O$_9$S calculated, 675.76; found, 676.16.

4.2.7. Synthesis of RGD nanoparticles

USPIO nanoparticles (56 mg, 1 mmol) was dispersed in 20 ml of toluene in a round-bottom flask, followed by mPPDA-silane (2.3 g, 1 mmol) being added to the solution and the resulting mixture was sonicated for 6 h at 50 °C. The product (PDA nanoparticles) was precipitated in hexane and isolated by centrifugation. The collected precipitation was dissolved in deionized water and purified by dialysis against deionzied water (MWCO = 12–14 K), to remove the free mPPDA-silane and others. Finally, PDA nanoparticles (20 µmol Fe) and RGD (13.5 mg, 20 µmol) were dissolved in 5 ml of DMF, and reacted under nitrogen for 6 h to obtain the RGD nanoparticles. The free RGD peptide and DMF were removed by dialysis against deionized water for 24 h.

4.2.8. Synthesis of FITC-RGD nanoparticles

FITC (10 µmol) and RGD nanoparticles (100 µmol Fe) were dissolved in DMF (10 ml) and then the mixture was stirred for 24 h at 4 °C. Subsequently, the free FITC and DMF were removed by dialysis against deionized water for 24 h. The obtained FITC-RGD nanoparticles were identified by UV–vis spectroscopy. It showed absorbance at 494 nm corresponding to FITC moiety.

4.3. TEM measurements

The average core size, size distribution and morphology were examined using a transmission electron microscope (Jeol JEM-2000 EX II, Japan) at a voltage of 100 kV. The composite dispersion was drop-cast onto a 200-mesh copper grid (Agar Scientific) and the grid was air-dried at room temperature before being loaded into the microscope.

4.4. SQUID magnetometer measurements

The magnetic properties of USPIO nanoparticles were studied using a SQUID magnetometer, obtained from Quantum Design (XL-7 magnetic property measurement system), at fields ranging from −10 to 10 kOe and at 25 °C.

4.5. Stability study of RGD nanoparticles

To examine the stability of the RGD nanoparticles, the resulting samples were tested with DLS and a 20 MHz relaxometer for a long period of time. The relaxivity of RGD nanoparticles in PBS buffer solution (pH 7.4) under physiological conditions and various pH solutions was investigated.

4.6. Relaxation time measurements

Relaxation times (T_1 and T_2) of an aqueous solution of RGD nanoparticles were measured to determine relaxivities, r_1 and r_2. All measurements were made using a relaxometer (NMS-120 Minispec, Bruker) operating at 20 MHz and $37.0 \pm 0.1\,°C$. Before each measurement, the relaxometer was tuned and calibrated. The values of r_1 and r_2 were determined from eight data points generated by inversion recovery and a Carr–Purcell–Meiboom–Gill pulse sequence, respectively. All of the experiments were repeated four times.

4.7. MR imaging study

RGD nanoparticles with various concentrations (400, 200, 100, 50 and 25 μM Fe) were prepared in PBS buffer solution with three different core sizes 13.1, 9.2, and 6.7 nm, respectively. T_2-weighted MR images of RGD nanoparticles were obtained on a 3.0 T MR scanner (Sigma; GE Medical Systems, Milwaukee, WI, USA) using a knee coil. T_2-weighted scanning was performed under the following conditions: fast gradient echo, repetition time (TR) = 5000 ms, echo delay time (TE) = 90 ms, flip angle = 10°, coronal view, and section thickness = 2 mm, FOV = 10 cm. All of the experiments were repeated four times.

4.8. Cell culture and animal model

MCF-7 (human breast adenocarcinoma cell line), A-549 (human lung adenocarcinoma epithelial cell line), HT-29 (human colon carcinoma cell line) and HT-1080 (human fibrosarcoma cell line) cells are all integrin receptor overexpressors (45–48). KB cells (human nasopharyngeal epidermal carcinoma cell line) lack integrin expression. All cells were obtained from the America Type Culture Collection (Manassas, VA, USA). MCF-7, A-549, HT-29 and HT-1080 cells were cultured in McCoy's 5A medium (GIBCO, NY, USA), Hybri-care medium (American Type Culture Collection) and supplemented with epidermal growth factor (Sigma; 30 ng ml^{-1}), Dulbecco's modified Eagle's medium (GIBCO, NY, USA), and L-15 medium (GIBCO, NY, USA), respectively. All media were supplemented with 10% fetal bovine serum, sodium bicarbonate (1.5 g l^{-1}), sodium pyruvate (1.0 mM), and nonessential amino acid (0.1 mM). All cells were cultured at 37 °C in a humidified 5% CO_2 atmosphere.

BALB/cAnN.Cg-Foxn1nu/CrlNarl mice (5 weeks old, male) were purchased from the National Laboratory Animal Center, Taipei, Taiwan. Animal experiments were performed in accordance with the institutional guidelines. The positive (MCF-7, A-549, HT-29 and HT-1080) and negative (KB) cells in 100 μl (10^6 cells) PBS were injected subcutaneously into four groups of nude mice. Cells were injected into the right (positive) and left (negative) lateral thighs of the mice. Each group contained five mice. An MR imaging experiment was performed one week after tumor implantation, at which time the tumors were measured to be at least 0.05–0.1 cm^3 in volume. This method produces a high yield of tumor in the lateral thighs of nude mice.

4.9. Cell cytotoxicity analysis

Before MR imaging study, the cell lines were used to measure the cell cytotoxicity of RGD nanoparticles. An amount of 10^5 cells was plated in each well of a 96-well plate 24 h before washing with PBS buffer solution (pH 7.4) and adding RGD nanoparticles at the desired concentrations (from 100 to 1000 μM Fe, 0.2 ml per well). Then, after 24 h of incubation, the supernatant was removed and cells were washed three times with PBS. Cell viability was then estimated using the MTT conversion test. Briefly, 50 μl of MTT solution was added to each well. After incubation for 2 h, each well was treated with DMSO (50 μl, 2.0 M). Absorption at 570 nm was measured on a plate reader. Each result was the average of three wells, and 100% viability was assumed for untreated cells.

4.10. Flow cytometry analysis

MCF-7, HT-29, A-549, HT-1080, and KB cells were seeded in six-well plates (each well 10^6 cells) and grown for 1 day. These cells were incubated with FITC-RGD nanoparticles (100 μl, 0.5 mM Fe) for 1 h and washed three times with PBS buffer solution. Finally, a total of 5×10^5 cells per sample were analyzed by flow-cytometric analysis (BD FACS Calibur, USA).

4.11. Confocal fluorescence microscopy

The MCF-7 cells were cultured on coverslips, which were kept in a 35 mm Petri dish for 15–24 h before treatment. After treatment with FITC-USPIO nanoparticles, FITC-RGD nanoparticles and RGD nanoparticles with four-fold excess free RGD at different times, the cells were washed with isotonic PBS buffer solution (pH 7.4), and then fixed with 4% paraformaldehyde solution in PBS buffer solution for 1 h at 37 °C. The coverslips were washed three times with PBS, and nonspecific binding sites were blocked in PBS containing 10% fetal bovine serum (FBS) and 0.2% Triton X-100 for 1 h. The coverslips were washed three times with buffer solution containing 0.2% triton X-100 in PBS. Cytoplasm of glycoproteins was stained with Hilyte Fluor^{TM} 594 acid (1:1000) in PBS for 30 min at 37 °C. Thereafter, the cells were washed three times with wash buffer. Subsequently, the nucleus of cells was incubated with Hoechst 33342 (1:200) in PBS buffer solution for 15 min at 37 °C. After staining, the samples were examined under a FluoView FV1000 confocal laser scanning microscope (Olympus UK Ltd), equipped with a UV laser (405 nm), an Ar laser (488 nm) and a HeNe laser (594 nm).

4.12. *In vitro* MR imaging study

T_2-weighted MR images of cell lines were taken using a 3.0 T MR scanner. All the cell lines were incubated with 13.1 nm RGD nanoparticles (diluted in 1 ml medium, 0.2 mM Fe) for 0.5 h at $37.0 \pm 0.1\,°C$ and washed three times with PBS. T_2-weighted scanning was performed under the following conditions: fast gradient echo, $TR = 5000$ ms, $TE = 90$ ms, flip angle $=10°$, coronal view, and section thickness $= 2$ mm, FOV $= 10$ cm. The contrast was calculated as (Fig. 8):

$$Contrast(\%) = \frac{SI_{post} - SI_{pre}}{SI_{pre}} \times 100\%$$

where SI_{pre} is the value of signal intensity for cells untreated with the contrast agent and SI_{post} is the value of signal intensity for cells treated with the contrast agent. All of the experiments were repeated four times.

4.13. *In vivo* MR imaging study

The *in vivo* MR imaging studies were carried out one week after tumor implantation. Mice were anesthetized with ketamine (3 ml kg^{-1}) and then RGD nanoparticles (13.1 nm; 15 μmol Fe kg^{-1})

were injected intravenously through the tail vein. The resulting of MR imaging was taken at 0.5–24 h after injection of RGD nanoparticles. The T_2-weighted scanning was performed under the following conditions of *in vitro* study and employing a high-resolution animal coil. $TR = 5000$ ms, $TE = 90$ ms, flip angle $= 10^o$, coronal view, and section thickness $= 3$ mm. The contrast was calculated as (Fig. 9):

$$\text{Contrast}(\%) = \frac{(SI_{post}/SI_{p.post}) - (SI_{pre}/SI_{p.pre})}{(SI_{pre}/SI_{p.pre})} \times 100\%$$

where SI_{post} is the signal intensity of after injection, $SI_{p.post}$ is the signal intensity of the phantom after injection, SI_{pre} is the signal intensity before injection, and $SI_{p.pre}$ is the signal intensity of the phantom before injection. All of the experiments were repeated four times.

4.14. Histology evaluation

Tumor-bearing mice were sacrificed after treatment with RGD nanoparticles and USPIO nanoparticles for 3 h. The tumors were removed through necropsy and preserved in 4% formaldehyde for 24 h. The tumors were dried and embedded in paraffin wax, processed for histology, and sliced onto four slides. First stained Prussian blue, the fixed cells were incubated with 10% potassium ferrocyanide in 10% hydrochloric acid for 1 h, and then stained with hematoxylin and eosin (H&E) according to standard clinical pathology protocols.

Acknowledgments

REFERENCES

1. Haubner R, Gratias R, Diefenbach B, Goodman SL, Jonczyk A, Kessler H. Structural and functional aspects of RGD-containing cyclic pentapeptides as highly potent and selectively integrin alphaV beta 3 antagonists. J Am Chem Soc 1996; 118(32): 7461–7472.
2. Koretz K, Schlag P, Boumsell L, Moller P. Expression of VLA-alpha 2, VLA-alpha 6 and VLA-beta 1 chains in normal mucosa and adenomas of the colon and in colon carcinomas and their liver metastases. Am J Pathol 1991; 138(3): 741–750.
3. Natali PG, Nicotra MR, Botti C, Mottolese M, Bigotti A, Segato O. Changes in expression of α6/β4 integrin heterodimer in primary and metastatic breast cancer. Br J Cancer 1992; 66(2): 318–322.
4. Zutter MM, Krigman HR, Santoro SA. Altered integrin expression in adenocarcinoma of the breast. Analysis by in situ hybridization. Am J Pathol 1993; 142(5): 1439–1448.
5. Albeda SM, Motto SA, Elder DE, Stewart RM, Damjanovich L, Herlyn M, Buck CA. Integrin distribution in malignant melanoma: association of the β3 subunit with tumor progression. Cancer Res 1990; 50(20): 6757–6764.
6. Gladson CL, Cheresh DA, Glioblastoma expression of vitronectin and the alpha v beta 3 integrin. Adhesion mechanism for transformed glial cells. J Clin Invest 1991; 88(6): 1924–1932.
7. Dobrucki LW, de Muinck ED, Lindner JR, Sinusas AJ. Approaches to multimodality imaging of angiogenesis. J Nucl Med 2010; 51(1): 66S–79S.
8. Wacker BD, Alford SK, Scott EA, Thakur MD, Longmore GD, Elbert DL. Endothelial cell migration on RGD-peptide-containing PEG hydrogels in the presence of sphingosine 1-phospahte. Biophysical J 2008; 94(1): 273–285.
9. Cai W, Shin DW, Chen K, Gheysens O, Cao Q, Wang SX, Gambhir SS, Chen X. Peptide labelled near infrared quantum dots for imaging tumor vasculature in living subjects. Nano Lett 2006; 6(4): 669–676.
10. Choy G, Choyke P, Libutti SK. Current advances in molecular imaging: noninvasive bioluminescent and fluorescent optical imaging in cancer research. Mol Imag 2003; 2(4): 303–312.
11. Erogbogbo F, Yong KT, Hu R, Law WC, Ding H, Chang CW, Prasad PN, Swihart MT. Biocompatible magnetofluorescent probes: luminescent silicon quantum dots coupled with superparamagnetic iron (III) oxide. ACS Nano 2010; 4(9): 5131–5138.
12. Chen X, Park R, Tohme M, Shahinian AH, Bading JR, Conti PS. Micro-PET and autoradiographic imaging of breast cancer alphaV-integrin expression using 18Fand 64Cu-labeled RGD peptide. Bioconjugate Chem 2004; 15(1): 41–49.
13. Janssen ML, Oyen WJ, Dijkgraaf I, Massuger LF, Frielink C, Edwards DS, Rajopadhye M, Boonstra H, Corstens FH, Boerman OC. Tumor targeting with radiolabeled alphavbeta3 integrin bind peptides in a nude mouse model. Cancer Res 2002; 62(21): 6146–6151.
14. Yu MK, Jeong YY, Park J, Park S, Kim JW, Min JJ, Kim K, Jon S. Drug-loaded superparamagnetic iron oxide nanoparticles for combined cancer imaging and therapy in vivo. Angew Chem Int Ed Engl 2008; 47(29): 5362–5365.
15. Jun Y-W, Huh Y-M, Choi J-S, Lee J-H, Song H-T, Kim S, Yoon S, Kim K-S, Shin J-S, Suh J-S, Cheon J. Nanoscale size effect of magnetic nanocrystals and their utilization for cancer diagnosis via magnetic resonance imaging. J Am Chem Soc 2005; 127(16): 5732–5733.
16. Bronstein LM, Huang X, Retrum J, Schmucker A, Pink M, Stein BD, Dragnea B. Influence of iron oleate complex structure on iron oxide nanoparticle formation. Chem Mater 2007; 19(15): 3624–3632.
17. Kwon SG, Piao Y, Park J, Angappane S, Jo Y, Hwang N-M, Park J-G, Hyeon T. Kinetics of monodisperse iron oxide nanocrystals formation by heating up process. J Am Chem Soc 2007; 129(42): 12571–12584.
18. Lee J-H, Huh Y-M, Jun Y-W, Seo J-W, Jang J-T, Song H-T, Kim S, Cho E-J, Yoon H-G, Suh J-S, Cheon J. Artificially engineered magnetic nanoparticles for ultra-sensitive molecular imaging. Nat Med 2007; 13(1): 95–99.
19. Jana NR, Chen Y, Peng X. Size- and shape-controlled magnetic (Cr, Mn, Fe, Co, Ni) oxide nanocrystals via a simple and general approach. Chem Mater 2004; 16(20): 3931–3935.
20. Park J, An K, Hang Y, Park JG, Noh H-J, Kim J-Y, Park J-H, Hwang N-M, Hyeon T. Ultra-large-scale syntheses of monodisperse nanocrystals. Nat Mater 2004; 3(12): 891–895.
21. Xie J, Chen K, Lee H-Y, Xu C, Hsu AR, Peng S, Chen X, Sun S. Ultrasmall c(RGDyK)-coated Fe3O4 nanoparticles and their specific targeting to integrin $\alpha_v\beta_3$-rich tumor cells. J Am Chem Soc 2008; 130(24): 7542–7543.
22. Wu P-C, Su C-H, Cheng F-Y, Weng J-C, Chen J-H, Tsai T-L, Yeh C-S, Su W-C, Hwu J-R, Tzeng Y, Shieh D-B. Modularly assembled magnetite nanoparticles enhances in vivo targeting for magnetic resonance cancer imaging. Bioconjugate Chem 2008; 19(10): 1972–1979.
23. Montet X, Funovics M, Montet-Abou K, Weissleder R, Josephson L. Multivalent effects of RGD peptides obtained by nanoparticle display. J Med Chem 2006; 49(20): 6087–6093.
24. Mornet S, Vasseur S, Grasset F, Duguet E. Magnetic nanoparticle design for medical diagnosis and therapy. J Mater Chem 2004; 14: 2161–2175.
25. Sun C, Veiseh O, Gunn J, Fang C, Hansen S, Lee D, Sze R, Ellenbogen RG, Olson J, Zhang M. In vivo MRI detection of gliomas by chlorotoxin–conjugated superparamagnetic nanoprobes. Small 2008; 4(3): 372–379.
26. Laurent S, Forge D, Port M, Roch A, Robic C, Elst LV, Muller RN. Magnetic iron oxide nanoparticles: synthesis, stabilization, vectorization, physicochemical characterizations, and biological applications. Chem Rev 2008; 108(6): 2064–2110.
27. Xie J, Xu C, Kohler N, Hou Y, Sun S. Controlled PEGylation of monodisperse Fe3O4 nanoparticles for reduced non-specific uptake by macrophage cells. Adv Mater 2007; 19(20): 3163–3166.
28. Vlerken LEV, Duan Z, Little SR, Seiden MV, Amiji MM. Biodistribution and pharmacokinetic analysis of paclitaxel and ceramide administered in multifunctional polymer-blend nanoparticles in drug resistant breast cancer model. Mol Pharm 2008; 5(4): 516–526.
29. Thünemann AF, Schütt D, Kaufner L, Pison, U, Möhwald H. Maghemite nanoparticles protectively coated with poly(ethylene imine) and poly(ethylene oxide)-block-poly(glutamic acid). Langmuir 2006; 22(5): 2351–2357.
30. Xie J, Huang J, Li X, Sun S, Chen X. Iron oxide platform for biomedical applications. Curr Med Chem 2009; 16(10): 1278–1294.

31. Chen K, Xie J, Xu H, Behera D, Michalski MH, Biswal S, Wang A, Chen X. Triblock copolymer coated iron oxide nanoparticles conjugate for tumor integrin targeting. Biomaterials 2009; 30(36): 6912–6919.

32. Sunderland CJ, Steiert M, Talmadge JE, Derfus AM, Barry SE. Targeted nanoparticles for detecting and treating cancer. Drug Dev Res 2006; 67(1): 70–93.

33. Veiseh O, Sun C, Gunn J, Kohler N, Gabikian, P, Lee D, Bhattarai N, Ellenbogen R, Sze R, Hallahan A, Olson J, Zhang M. Optical and MRI multifunctional nanoprobe for targeting gliomas. Nano Lett 2005; 5(6): 1003–1008.

34. Cheng C-M, Chu P-Y, Chuang K-H, Roffler S, Kao C-H, Tseng W-L, Shiea J, Chang W-D, Su Y-C, Chen B-M, Wang Y-M, Cheng T-L. Hapten-derivatized nanoparticle targeting and imaging of gene expression by multimodality imaging systems. Cancer Gene Ther 2009; 16(1): 83–90.

35. Chen T-J, Cheng T-H, Chen C-Y, Hsu SCN, Cheng T-L, Liu G-C, Wang Y-M. Targeted herceptin–dextran iron oxide nanoparticles for noninvasive imaging of HER2/neu receptors using MRI. J Biol Inorg Chem 2009; 14(2): 253–260.

36. Chen T-J, Cheng T-H, Hung Y-C, Lin K-T, Liu G-C, Wang Y-M. Targeted folic acid-PEG nanoparticles for noninvasive imaging of folate receptor by MRI. J Biomed Mater Res A 2008; 87A(1): 165–175.

37. Lee H, Lee E, Kim DK, Jang NK, Jeong YY, Jon S. Antibiofouling polymer-coated superparamagnetic iron oxide nanoparticles as potential magnetic resonance contrast agents for in vivo cancer imaging. J Am Chem Soc 2006; 128(22): 7383–7389.

38. Zugates GT, Anderson DG, Little SR, Lawhorn IEB, Langer R. Synthesis of poly(β-amino ester)s with thiol reactive side chains for DNA delivery. J Am Chem Soc 2006; 128(39): 12726–12734.

39. Kohler N, Fryxell GE, Zhang M. A bifunctional poly(ethylene glycol) silane immobilized on metallic oxide-based nanoparticles for conjugation with cell targeting agents. J Am Chem Soc 2004; 126(23): 7206–7211.

40. Kohler N, Sun C, Fichtenholtz A, Gunn J, Fang C, Zhang M. Methotrexate-immobilized poly(ethylene glycol) magnetic nanoparticles for MR imaging and drug delivery. Small 2006; 2(6): 785–792.

41. Kohler N, Sun C, Wang J, Zhang M. Methotrexate-modified superparamagnetic nanoparticles and their intracellular uptake into human cancer cells. Langmuir 2005; 21(19): 8858–8864.

42. Zhang Y, Kohler N, Zhang M. Surface modification of superparamagnetic magnetite nanoparticles and their intracellular uptake. Biomaterials 2002; 23(7): 1553–1561.

43. Zhang C, Jugold M, Woenne EC , Lammers T, Morgenstern B, Mueller MM, Zentgraf H, Bock M, Eisenhut M, Semmler W, Kiessling F. Specific targeting of angiogenesis by RGD-conjugated ultrasmall superparamagnetic iron oxide particles using a clinical 1.5-T magnetic resonance scanner. Cancer Res 2007; 67(4): 1555–1562.

44. Reynolds F, O'Loughlin T, Weissleder R, Josephson L. Method of determining nanoparticle core weight. Anal Chem 2005; 77(3): 814–817.

45. Deryugina EI, Bourdon MA, Jungwirth K, Smith JW, Strongin AY. Functional activation of integrin $\alpha_v\beta_3$ in tumor cells expressing membrane-type 1 matrix metalloproteinase. Int J Cancer 2000; 86(1): 15–23.

46. Odrljin TM, Haidaris CG, Lerner NB, Simpson-Haidaris PJ. Integrin $\alpha_v\beta_3$ mediated endocytosis of immobilized fibrinogen by A549 lung alveolar epithelial cells. Am J Respir Cell Mol Biol 2001; 24(1): 12–21.

47. Veeravagu A, Liu Z, Niu G, Chen K, Jia B, Cai W, Jin C, Hsu AR, Connolly AJ, Tse V, Wang F, Chen X. Integrin $\alpha_v\beta_3$-targeted radioimmunotherapy of glioblastoma multiforme. Clin Cancer Res 2008; 14(22): 7330–7339.

48. Garrigues HJ, Rubinchikova YE, Persio MD, Rose TM. Integrin $\alpha_v\beta_3$ binds to the RGD motif of glycoprotein B of kaposi's sarcoma-associated herpesvirus and functions as an RGD-dependent entry receptor. J Virol 2008; 82(3): 1570–1580.